Identification of Resistivity Distributions in Dielectric Layers by Measurement Model Analysis of Impedance Spectroscopy

Yu-Min E Chen, Anh E Nguyen, Mark E. Orazem, Bernard E Tribollet,
Nadine E Pébère, Marco E Musiani, Vincent Vivier

Identification of Resistivity Distributions in Dielectric Layers by Measurement Model Analysis of Impedance Spectroscopy

Yu-Min Chen[a], Anh Son Nguyen[b], Mark E. Orazem[a,*], Bernard Tribollet[c], Nadine Pébère[b], Marco Musiani[d], Vincent Vivier[c]

[a]*Department of Chemical Engineering, University of Florida, Gainesville, FL, 32611, USA*
[b]*Université de Toulouse, CIRIMAT, UPS/INPT/CNRS, ENSIACET, 31030 Toulouse cedex 4, France*
[c]*LISE, UMR 8235 du CNRS, Université P. et M. Curie, CP 133, 4 Place Jussieu, 75252 Paris cedex 05, France*
[d]*ICMATE, CNR, Corso Stati Uniti 4, 35127 Padova, Italy*

Abstract

The Voigt measurement model, developed in the 1990s for identification of the error structure of impedance measurements, is shown here to have utility in identifying resistivity distributions that give rise to frequency dispersion. The analysis was validated by application to synthetic data derived from a constant–phase–element model, a power–law distribution of resistivity, and an exponential distribution corresponding to a Young impedance. The application to experimental data obtained from coated aluminum demonstrates its utility for interpretation of impedance measurements.

Keywords: Constant–Phase Elements (CPE); power–law model; Young impedance; organic coatings; passive oxides

1. Introduction

The origin of the constant–phase element can be attributed to the distribution of time constants along or normal to the electrode surface. The impedance response for the distribution of time constants along the electrode surface can be expressed by the model developed by Brug et al. [1] Several different models have been proposed for the impedance associated with a resistivity distribution normal to electrode surface. Young [2] assumed that the nonstoichiometry of the oxide layer resulted in an exponential variation of the resistivity. Under the assumption of a uniform dielectric constant, Hirschorn et al. [3] proposed a power–law distribution of resistivity to relate constant–phase–element parameters to film properties.

Impedance spectroscopy has been applied to the study of resistivity distributions in oxide films. Young showed that the impedance response of oxides on niobium may be explained in terms of an exponential distribution of resistivity.[2, 4] Bataillon and Brunet[5] attributed dispersion in the impedance response of oxide films formed by high–temperature water oxidation of zircaloy 4 to oxide film defects and transport. Orazem et al. [6] demonstrated the application of a power-law distribution of resistivity to extract the thickness of oxide films on 18Cr-8Ni stainless steel

---

*Corresponding author
Email address: meo@che.ufl.edu (Mark E. Orazem)

and X12CrNiMoV12-3 steel. They also verified the power-law distribution of resistivity for split-thickness human cadaver skin (300-400 μm thick). Not all authors have concluded that CPE behavior for oxides may be attributed to normal distribution of film properties. Mohammadi et al. [7] reported that the formula of Brug et al. [1] provided the best correlation to independently measured thicknesses of oxide films on 304 stainless steel.

Electrochemical impedance spectroscopy methods have also been used widely to assess the corrosion protection performance of coatings. Beaunier et al. [8] proposed a general model in which the ohmic resistance is in series with the parallel combination of the capacitance of the polymer coating and the electrolyte resistance in the pores; the latter is in series with the parallel combination of double layer capacity and faradaic impedance of the wet area at the metal/coating interface. This model was modified by Mansfeld [9], who replaced the faradaic impedance of the corrosion process with a polarization resistance. The faradaic impedance of Beaunier et al. [8] was treated by Hirayama and Haruyama [10] in terms of quantities that accounted for the parallel contributions of reactions at the metal/coating interface and at exposed metal surface by pores or coating defects. Upadhyay et al. [11] found that impedance responses of glycidyl carbamate functional coatings were closely related to structural and compositional variations. In addition, they related single–frequency impedance measurements to water uptake.

Hu et al. [12] showed that the impedance of epoxy–coated aluminum alloy LY12 in 3.5% NaCl solution was sensitive to the time–dependent uptake of water, oxygen and chloride ions. Metroke et al. [13] showed that impedance of organically modified silane thin films on 2024-T3 aluminum alloy in 0.05% NaCl or 0.5 M K_2SO_4 was sensitive to water and electrolyte uptake as well as to degradation of coating properties. Kittel et al. [14, 15] used embedded electrodes to demonstrate marked variations in the impedance of organic coatings as a function of depth, concluding that accurate models for coated electrodes should integrate gradients of properties over the thickness of the coatings. However, those authors did not propose any specific resistivity or permittivity profiles.

Hinderliter et al. [16] used a two–layer representation of coating changes due to water intrusion and known effective medium theories for dielectric and resistivity changes to predict changes in impedance spectra seen in immersion or other accelerated testing of coating films. Amand et al. [17] developed a model for the impedance of coatings based on the assumptions that the coating uptakes electrolyte such that the volume fraction of the electrolyte varies along the coating thickness according to a power-law, the resistivity and permittivity profiles of the electrolyte-penetrated coating can be calculated through an effective medium theory (EMT) formula corresponding to a parallel combination of the two media (electrolyte and coating material), and some pores extend from the coating/electrolyte interface to the substrate/coating interface, providing a low resistance path. Their work showed that, of the effective medium theories proposed by Hinderliter et al. [16], linear combinations provided results that were consistent with the observed impedance response. Musiani et al. [18] demonstrated that, although resistivity profiles may be obtained using effective medium theory and linear combinations of conductivities/permittivities, the fitted water uptake values are not reliable because the real composition of the solution that penetrates the coating is unknown.[12, 19] Nguyen et al. [20] suggested that a dry epoxy-polyaminoamide waterborne paint coating on a 2024 aluminium alloy showed constant–phase–element behavior that could be modeled accurately with the power–law model. However, for the same coating immersed in either a 0.5 M or a 0.05 M NaCl solution, the Young impedance model provided a better fit to the impedance data.

The Voigt series, used by Agarwal et al. as a measurement model to identify the error structure of impedance measurements[21–23], has been employed to identify a distribution of relaxation time

constants corresponding to a given impedance spectrum.[24, 25] In the present paper, a systematic method, based on the Voigt measurement model, is proposed to analyze the resistivity distribution for synthetic impedance data and for experimental data obtained for anti–corrosion coatings.

2. Theoretical Development

This section summarizes the use of the measurement model for the assessment of resistivity distribution in films, previously described by Hirschorn et al. [3] The resistivity distribution can be derived from the Voigt element parameters, τ_i and R_i. The corresponding impedance is expressed as

$$Z_{\mathrm{RC}} = \sum_{i=1}^{k} \frac{R_i}{1 + j\omega\tau_i} \tag{1}$$

where each Voigt element represents the time constant and resistivity for a given differential element. The number of Voigt elements k is increased sequentially under the constraint that the 95.4 % confidence interval for each regressed parameter does not include zero.[21] Each RC–time constant is assumed to be associated with a differential layer of the film.

The differential capacitance, defined to be

$$C_i = \tau_i/R_i \tag{2}$$

is a function of dielectric constant and the thickness of the element. The corresponding thickness of each element i, d_i, is related to the local dielectric constant ε_i by

$$d_i = \frac{\varepsilon_i \varepsilon_0}{C_i} \tag{3}$$

where $\varepsilon_0 = 8.8542 \times 10^{-14}$ F/cm is the permittivity of vacuum. The local resistance can also be related to thickness of element i by

$$R_i = \rho_i d_i \tag{4}$$

Therefore, the time constant τ_i is independent of element thickness and can be expressed as

$$\tau_i = \rho_i \varepsilon_i \varepsilon_0 \tag{5}$$

Under the assumption that dielectric constant is uniform, the variability of capacitance could be the consequence of a changing element thickness. Based on equations (4) and (5), the resistivity, R_i, could also be related to the time constant by

$$\rho_i = \frac{R_i}{d_i} = \frac{\tau_i}{\varepsilon \varepsilon_0} \tag{6}$$

The elements with smallest and largest resistivity values were assumed to be located at the interfaces of the system, and the resistivity of elements in the system was assumed to increase or decrease monotonically. Thus, if the thickness of the element with the smallest resistivity value is d_1 and the element with the second smallest resistivity value is d_2, the specific position of element with second smallest resistivity value in the system is $d_1 + d_2$. The specific position of other elements in systems can be calculated in the same manner.

3

3. Experimental

The coating samples and the protocol for impedance measurement were described in detail by Nguyen et al. [26] The following section summarizes the essential features.

3.1. Materials

The coating was a two-component water-based paint manufactured by Mapaero SAS, used as an anti-corrosive primer. It consisted of a polyaminoamide (Versamid type) base and a bisphenol A epoxy polymer hardener. Coatings henceforth called CC contained the following pigments: titanium oxide (12 wt.%), talc (11 wt.%), silica (1 wt.%) and strontium chromate (16 wt.%). Other coatings, henceforth called NCC, contained a mixture of zinc oxide and a phosphosilicate (10 wt.%) to replace $SrCrO_4$ as inhibitive pigment. In both cases, the ratio of the pigment volume concentration (PVC) to critical pigment volume concentration (CPVC) was 0.61. The coating preparation was that described in references [20] and [26]. Before painting, the 2024 T3 aluminium alloy samples were degreased at 60 °C (pH = 9) for 15 minutes, rinsed twice with distilled water, then etched in an acid bath at 52 °C for 10 minutes, and rinsed again with distilled water. The liquid paints were applied by air spraying. After curing at 60 °C, the coatings were $18 - 22$ μm thick.

3.2. Impedance Measurements

Nguyen et al. [26] measured the impedance of coating in two different configurations: metal–coating–metal (dry coating) and metal–coating–electrolyte. In the present paper, only impedance results obtained with dry coatings are re-examined. Dry coatings were examined either as–prepared or as aged samples. The aging process consisted of immersion in 0.5 M NaCl solution for about 1 month and successive drying at room temperature in air for up to 12 months. The impedance of dry coatings was measured in a two–electrode configuration. A cylindrical Plexiglass tube was fixed on top of the coated sample, exposing a surface area of 5.94 cm^2, and filled with Hg into which a Cu wire was dipped to create electrical contact. Impedance measurements, carried out using a Solartron 1255 Frequency Response Analyzer and a 1296 Dielectric Interface, were obtained with a 0 V dc bias and a 100 mV peak–to–peak sinusoidal perturbation. Frequency was swept downwards from 10^5 Hz to 1 Hz, recording 10 points per decade. Since the signal–to–noise ratio worsened below 1 Hz, lower frequencies were not investigated.

4. Results and Discussion

To validate the method to extract resistivity distributions, the measurement model analysis was applied to synthetic impedance data generated for a constant–phase element, for a power–law distribution of resistivity, and for the Young model, corresponding to an exponential distribution of resistivity. The method was then applied to experimental impedance data obtained for dry coatings on an AA2024 aluminum alloy.

4.1. Synthetic Constant–Phase–Element Data

Synthetic data were generated following

$$Z_{\text{CPE}} = \frac{1}{(j\omega)^\alpha Q} \tag{7}$$

where α and Q are parameters representative of a constant–phase element. Equation (7) is representative of a blocking system with an infinite low–frequency impedance. When $\alpha = 1$, the system is described by a single time constant and the parameter Q has units of capacitance; otherwise, Q has units of $\mathrm{F/s}^{1-\alpha}\mathrm{cm}^2$.

Synthetic impedance data were created using equation (7) with addition of random normally distributed stochastic noise with a standard deviation equal to 0.2 percent of the modulus of the impedance. The parameter Q was assigned a value $Q = 1 \times 10^{-6}$ $\mathrm{F/s}^{1-\alpha}\mathrm{cm}^2$. The real part Z_r and the imaginary part Z_j of the synthetic impedance were obtained from

$$Z_\mathrm{r} = Z_\mathrm{r,CPE} + 0.002\,|Z|\,p\,(0,1) \tag{8}$$

and

$$Z_\mathrm{j} = Z_\mathrm{j,CPE} + 0.002\,|Z|\,p\,(0,1) \tag{9}$$

respectively, where $|Z|$ is the magnitude of the impedance and $p(0,1)$ is the probability density function with mean equal to zero and with standard deviation equal to unity. The exponent α was treated as a parameter with values of 0.67, 0.8 and 0.95. The magnitude and the ohmic–resistance–corrected phase angle are presented in Figures 1(a) and 1(b), respectively. The lines in these figures represent the fit of the measurement model given as equation (1). The adjusted phase angle shown in Figure 1(b) can be expressed as

$$\varphi = \tan^{-1}\left(\frac{Z_\mathrm{j}}{Z_\mathrm{r} - R_\mathrm{e}}\right) \tag{10}$$

where R_e is the ohmic resistance. In the present case, the ohmic resistance was assigned a value of zero; thus, the phase angle calculated from equation (10) was equivalent to the usual phase angle.

The error structure model employed, in which the standard deviation of the impedance is given as $\sigma = 0.002\,|Z|$, is in agreement with the error structures obtained under potentiometric modulation.[22, 27] The results presented in Figure 1(a) suggest that addition of the random noise does not have visible effects on the impedance data. Figure 1(b) suggests that the ohmic–resistance–corrected phase angle is more sensitive to the added noise, but the effects are small.

Hirschorn et al. [3] observed that the resistivity distribution corresponding to a CPE follows a power law, e.g.,

$$\frac{\rho}{\rho_\delta} = \xi^{-\gamma} \tag{11}$$

where ρ_δ is the boundary value of resistivity at the film–electrolyte interface and γ is related to α such that
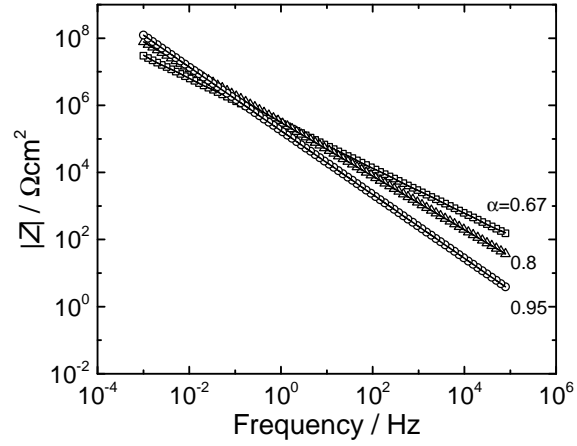
$$\alpha = \frac{\gamma - 1}{\gamma} \tag{12}$$

$\xi = x/\delta$, and δ is the thickness of the film. The value of film thickness was obtained from the regressed measurement model parameters following
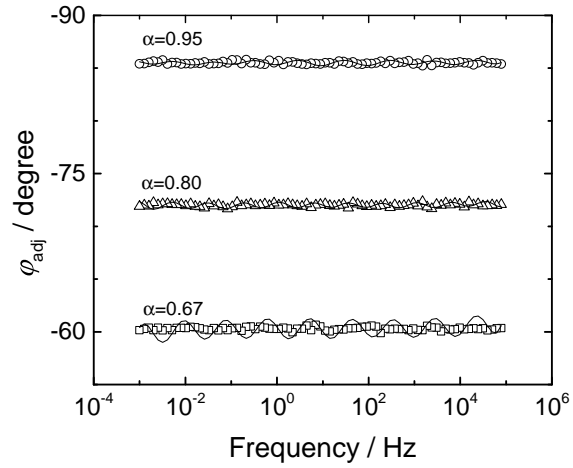
$$\delta = \sum_{i=1}^{n} d_\mathrm{i} \tag{13}$$

where n is the maximum number of Voigt elements. The position variable x corresponding to element k was obtained from

$$x_\mathrm{k} = \sum_{i=1}^{k} d_\mathrm{i} \tag{14}$$

5

(a)

(b)

Figure 1: Synthetic impedance spectra calculated from equations (7), (8), and (9) with $Q = 1 \times 10^{-6}$ F/s$^{1-\alpha}$cm^2 and α as a parameter: a) magnitude of impedance and b) ohmic–resistance–corrected phase angle calculated from equation (10). The lines represent the measurement model fit.
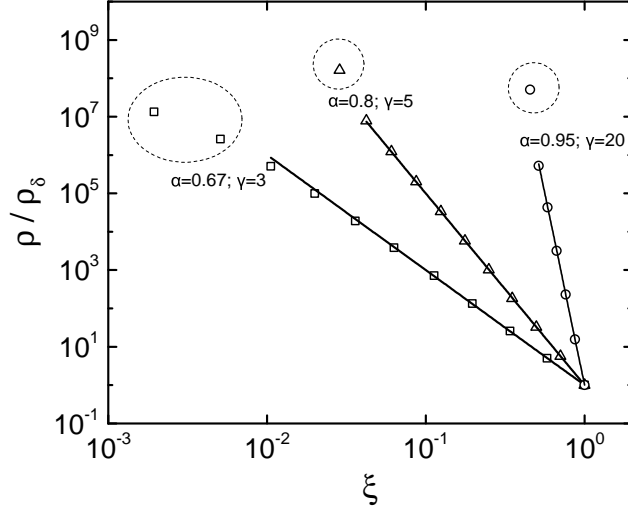
Figure 2: Resistivity corresponding to the synthetic data presented in Figure 1 scaled by ρ_δ and presented as a function of dimensionless position. Symbols are the discrete resistivity values calculated from equation (6) using the regressed values of τ_i under the assumption that $\varepsilon = 12$. The circled values were not used to estimate the slopes reported in Table 1. The lines represent the distribution used to generate the synthetic data.

Table 1: Results of the measurement model analysis of the synthetic CPE model data.

γ input	3	5	20
γ regressed	2.86	5.02	19.82

The parameter ρ_δ is the resistivity at $\xi = 1$ or $x = \delta$.

The resistivity distribution developed from the measurement model analysis is presented in Figure 2 for the synthetic CPE data shown in Figure 1. A value of ρ_δ cannot be obtained from CPE data; thus, the measurement model analysis provides only the expected value for the exponent in the power–law distribution. As shown by Hirshorn et al.,[3] the measurement model parameters corresponding to the end of the impedance spectrum are often not continuous with the other parameters; thus, the regressed measurement model parameters corresponding to the highest time constant were not included in the estimate of the resistivity distribution.

The results presented in Figure 2 are in agreement with the analysis presented by Hirschorn et al. [3] for the CPE. The input values of γ corresponding to equation (12) and the regressed values are shown in Table 1. These results show good agreement between input and output values of γ. While the added noise was used to mimic experimental data, similar results were obtained for noise–free synthetic data.

4.2. Synthetic Power–Law Model Data

Hirschorn et al. [3] proposed a distribution of resistivity that provided a power–law distribution with bounded values for resistivity to be

$$\frac{\rho}{\rho_\delta} = \left(\frac{\rho_\delta}{\rho_0} + \left(1 - \frac{\rho_\delta}{\rho_0} \right) \xi^\gamma \right)^{-1} \tag{15}$$

where ρ_0 and ρ_δ are the boundary values of resistivity at the interfaces. Under the assumption that the dielectric constant is uniform, the impedance of the film can be written for an arbitrary resistivity distribution $\rho(x)$ as

$$Z_f(\omega) = \int_0^\delta \frac{\rho(x)}{1 + j\omega\varepsilon\varepsilon_0\rho(x)} \, dx \tag{16}$$

Following equation (15), a general expression of the impedance can be given as

$$Z_f(\omega) = g \frac{\delta\rho_\delta^{1/\gamma}}{\left(\rho_0^{-1} + j\omega\varepsilon\varepsilon_0 \right)^{(\gamma-1)/\gamma}} \tag{17}$$

where

$$g = 1 + 2.88\gamma^{-2.375} \tag{18}$$

Equation (17) is in the form of a CPE if $\omega > (\rho_0\varepsilon\varepsilon_0)^{-1}$, i.e.,

$$Z_f(\omega) = g \frac{\delta\rho_\delta^{1/\gamma}}{(j\omega\varepsilon\varepsilon_0)^{(\gamma-1)/\gamma}} = \frac{1}{(j\omega)^\alpha Q} \tag{19}$$

Therefore, equation (17) has CPE behavior for $(\rho_0\varepsilon\varepsilon_0)^{-1} < \omega < (\rho_\delta\varepsilon\varepsilon_0)^{-1}$.

Synthetic data were generated using equation (17) for different values of ρ_0 and γ. The dielectric constant was given a value of 10, the film thickness was $\delta = 100$ nm, and the term ρ_δ was assigned a value of 100 Ωcm. The corresponding characteristic frequency was

$$f_\delta = \frac{1}{2\pi\rho_\delta\varepsilon\varepsilon_0} = 1.8 \text{ GHz} \tag{20}$$

which was outside the frequency range of the synthetic data. Noise was added following the protocol expressed as equations (8) and (9). Regressed values for measurement model parameters were used to generate resistivity distributions which were in turn regressed by equation (11) to obtain values of γ.

If the value of ρ_0 in equation (17) is close to $(\omega\varepsilon\varepsilon_0)^{-1}$, neither term in the denominator of equation (17) can be neglected. An example is presented in Figure 3. The characteristic frequency corresponding to ρ_0 for Figure 3 is given as

$$f_0 = \frac{1}{2\pi\rho_0\varepsilon\varepsilon_0} = 0.18 \text{ Hz} \tag{21}$$

This value is very close to the highlighted symbol in Figure 3.

The magnitude of the synthetic impedance data and the ohmic–resistance–corrected phase angle obtained from equation (17) are presented in Figure 4(a) and 4(b), respectively, with ρ_0 as a parameter. The added noise is barely visible in Figures 4(a) and 4(b).
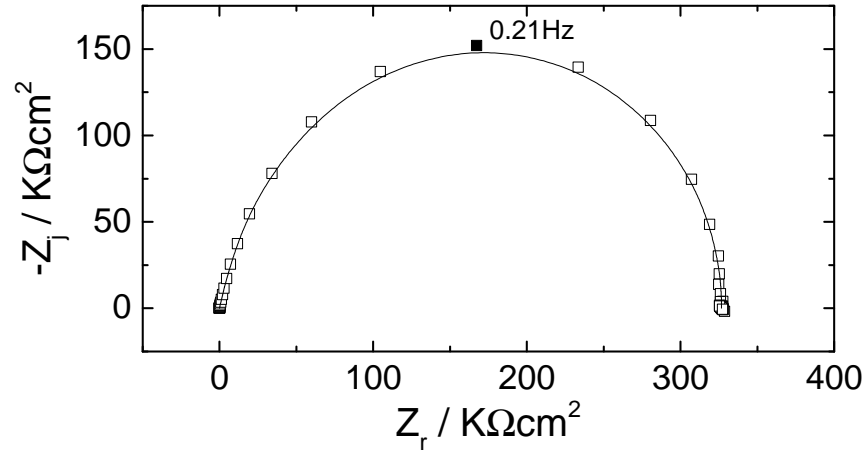
8

Figure 3: Nyquist representation of the impedance by equation (17) with parameters $\rho_0 = 10^{12}$ Ωcm, $\rho_\delta = 100$ Ωcm, $\varepsilon = 10$, $\delta = 100$ nm and $\gamma = 6.67$. The solid line represents the regression of equation (1) to the synthetic data.

(a)

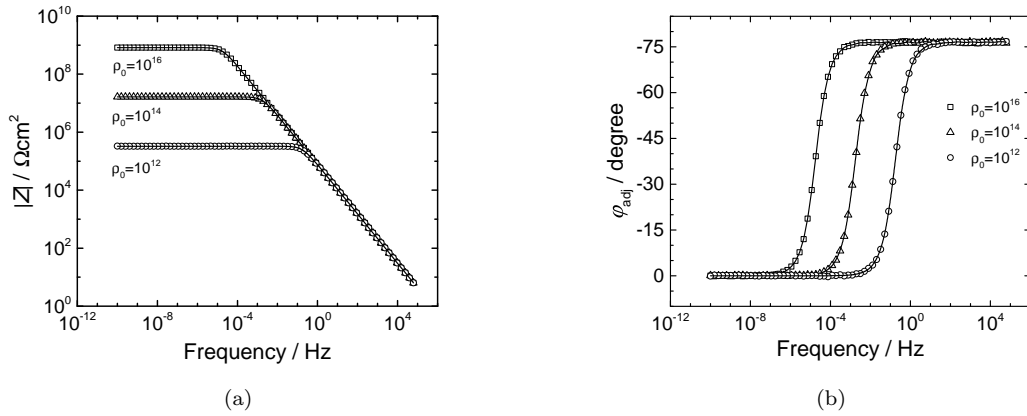(b)

Figure 4: Synthetic impedance data obtained from (17) with $\rho_\delta = 100$ Ωcm, $\varepsilon = 10$, $\delta = 100$ nm, $\gamma = 6.67$, and ρ_0 in units of Ωcm as a parameter: a) magnitude of impedance and b) ohmic–resistance–corrected phase angle. The lines represent the regression of equation (1) to the data.
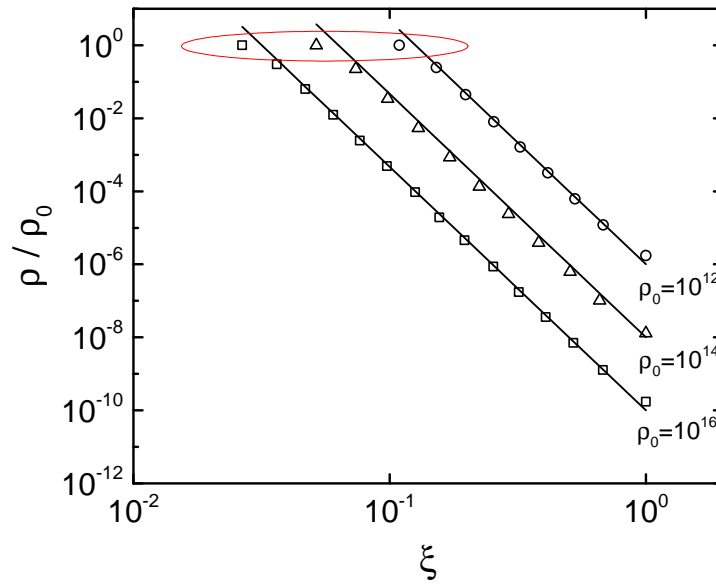
Figure 5: Dimensionless resistivity as a function of dimensionless position for synthetic impedance data in Figure 4. The symbols are the discrete resistivity values calculated from equation (6) using the regressed values of τ_i and $\varepsilon = 10$. The lines represent the distribution used to generate the synthetic data. The circled values are close to unity, suggesting that the measurement model provide a good estimate for ρ_0.

Table 2: Results of the measurement model analysis of the synthetic power–law model data.

γ input	6.67	6.67	6.67
γ regressed	6.11	6.58	6.50
ρ_0 input, Ωcm	1×10^{16}	1×10^{14}	1×10^{12}
ρ_0 regressed, Ωcm	0.78×10^{16}	0.77×10^{14}	0.77×10^{12}

The resistivity distribution functions for the synthetic impedance presented in Figure 4(a) are shown in Figure 5. The resistivity in Figure 5 is nondimensionalized by ρ_0, instead of ρ_δ as used in Figure 2. The values of circled points in Figure 5 are very close to unity, suggesting that the largest resistivity values obtained from (17) are very close to ρ_0.

The input values and the regressed values of γ and ρ_0 are shown in Table 2. These results show good agreement between input and output values of γ. The regressed values of ρ_0 are in fair agreement with input values. Extraction of values for $\rho_0 > 10^{12}$ Ωcm was possible only for frequencies that are much smaller than generally measured. The results presented here are used solely to demonstrate the utility of the measurement model approach to extract parameters consistent with input values.

4.3. Synthetic Young Impedance Data

The impedance proposed by Young [2, 4] can be expressed as

$$Z_{\mathrm{Y}} = -\frac{\lambda}{\mathrm{j}\omega\varepsilon\varepsilon_0} \ln\left(\frac{1 + \mathrm{j}\omega\varepsilon\varepsilon_0\rho_0 e^{-\delta/\lambda}}{1 + \mathrm{j}\omega\varepsilon\varepsilon_0\rho_0}\right) \tag{22}$$

based on exponential variation of resistivity that can be expressed as

$$\rho(x) = \rho_0 \exp\left(-\frac{x}{\lambda}\right) \tag{23}$$

or, in terms of dimensionless position,

$$\rho(\xi) = \rho_0 \exp\left(-\frac{\delta}{\lambda}\xi\right) \tag{24}$$

A Young impedance behavior, with this type of resistivity distribution, has been seen in epoxy–polyaminoamide waterborne paint in contact with 0.5 M NaCl by Nguyen et al. [20, 26]

The synthetic Young impedance data calculated following equation (22) with 0.2 percent of normally random distributed noise and with δ/λ and ρ_0 as independent parameters are presented in Figure 6. As shown in Figures 6(a) and 6(b), respectively, the added noise did not have visible effect on either the magnitude and phase angle of synthetic Young impedance data.

The resistivity distribution obtained from regression of equation (1) for synthetic Young impedance data is shown in Figure 7 as a function of dimensionless position, ξ, with ρ_0 and δ/λ as parameters. A smaller number of Voigt elements were needed to fit synthetic Young impedance data with a small value of δ/λ. For $\delta/\lambda = 8$, seven Voigt elements were needed; whereas, for $\delta/\lambda = 2$ only three Voigt elements could be obtained. The input values and the regressed values of ρ_0 and δ/λ are shown in Table 3. In agreement with equation (23), values of resistivity scaled to ρ_0 superpose for given values of δ/γ, as shown in Figure 8.
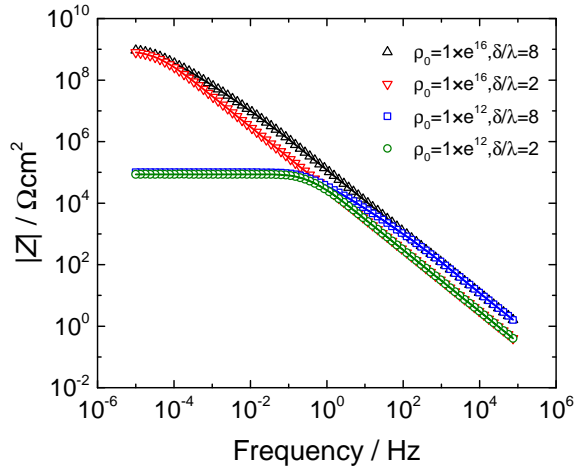
(a)
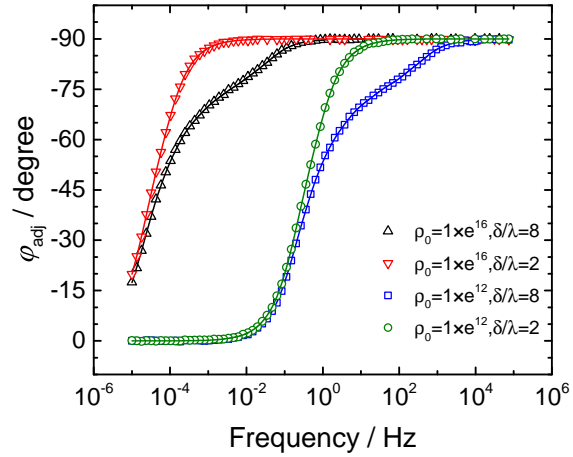
(b)

Figure 6: Synthetic Young impedance data calculated following equation (22) with 0.2 percent of normally random distributed noise and with δ/λ and ρ_0 as independent parameters: a) magnitude of impedance and b) ohmic–resistance–corrected phase angle. The lines represent the regression of equation (1) to the data.
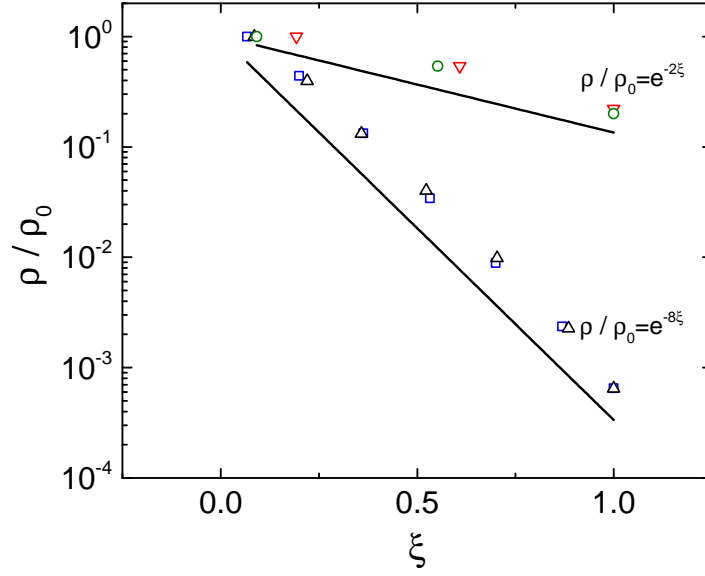
Figure 7: Resistivity as a function of dimensionless position. The symbols are the discrete resistivity values calculated from equation (6) using the regressed values of τ_i and $\varepsilon = 4.5$. The lines represent the distribution used to generate the synthetic data.

Table 3: Input values and regressed values for measurement model analysis of synthetic impedance data based on the Young model.

ρ_0, Ωcm		δ/λ	
input	regressed	input	regressed
1×10^{16}	1.3×10^{16}	8	6.5
1×10^{16}	1.2×10^{16}	2	1.7
1×10^{12}	1.4×10^{12}	8	7.1
1×10^{12}	1.2×10^{12}	2	1.5
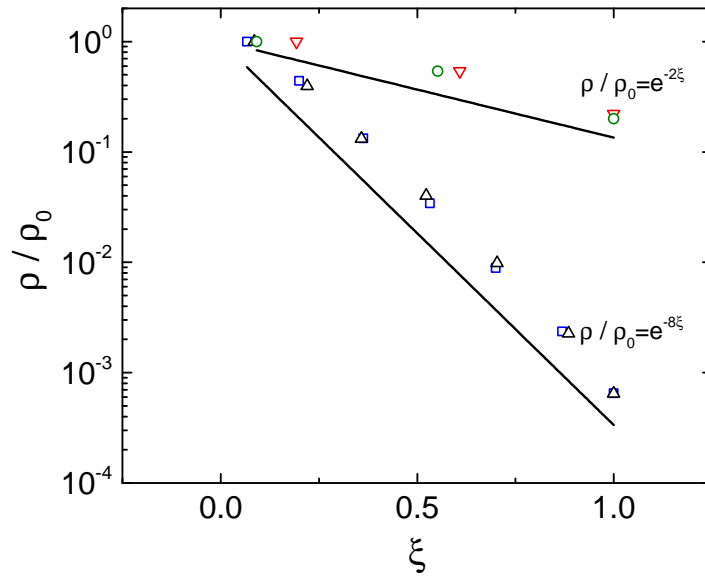
Figure 8: Dimensionless resistivity as a function of dimensionless position. The symbols are those used in Figure (7) for the discrete resistivity values calculated from equation (6) using the regressed values of τ_i and $\varepsilon = 4.5$. The lines represent the distribution used to generate the synthetic data.

4.4. Experimental Impedance Data

The analysis discussed above was applied to impedance data for dry coating samples, collected by Nguyen et al.[20, 26] The magnitude and ohmic–resistance–corrected phase angle for as–prepared and aged CC coating on 2024 aluminium alloy are presented in Figure 9. The impedance magnitude for the aged CC coating, shown in Figure 9(a), is about 3 times smaller than the impedance for the as–prepared CC coating. The ohmic–resistance–corrected phase angle of the as–prepared CC coating had a value close to 89° over a five–decade frequency, suggesting a CPE behavior. In contrast, the ohmic–resistance–corrected phase angle of aged CC decreased from about 88° at 10^5 Hz to about 80° at 1 Hz, suggesting that the properties of CC coating were severely and irreversibly affected after ageing and were no longer compatible with CPE behavior.

The measurement model was fit to the data presented in Figure 9, and the analysis described in equation (3) to (6) was used to identify the corresponding resistivity distribution. The resistivity distribution was obtained under the assumption that the dielectric constant may be assumed to be uniform. As shown in Figure 8 of Nguyen et al.,[20] the dielectric constant does not change appreciably with water uptake (a factor of two or three) and cannot account for the large range of time constants evident in the impedance response. Musiani et al. [28] have shown that a variation of dielectric constant in the region in which the resistivity is small has no effect on the impedance response.

Thus, the dielectric constant was assumed to be uniform with a value of $\varepsilon = 4.9$ as suggested by Nguyen et al. [20, 26] The resulting resistivity distribution is presented in Figure 10(a) for the as–prepared coating and Figure 10(b) for the aged coating. The position coordinate for the as–prepared coating presented in Figure 10(a) is in a logarithmic coordinate, and the resulting straight line is in agreement with a CPE or power–law behavior with $\gamma = 63$ and, following equation (12), $\alpha = 0.984$. This value is very close to the value of $\alpha = 0.987$ reported by Nguyen et al. [20, 26].

The low–frequency variation of phase angle for the as–prepared coating, evident in Figure 9(b), was attributed by Nguyen et al. [20] to the influence of the bulk resistivity ρ_0, as seen in equation (17). As shown in Figure 5, the resistivity distribution obtained by the measurement model analysis appears as a straight line in log–log coordinates, with the largest value close to ρ_0. Thus, the results presented in Figure 10(a) are consistent with the use of equation (17).

In the case of aged CC coating, presented in Figure 10(b), a model is proposed in which the resistivity follows an interpolation formula given as

$$\rho = \left(\frac{1}{\rho_{0,1} \exp\left(-\left(\frac{\delta}{\lambda}\right)_1 \xi\right)} + \frac{1}{\rho_{0,2} \exp\left(-\left(\frac{\delta}{\lambda}\right)_2 \xi\right)} \right)^{-1} \tag{25}$$

Equation (25) may be considered to represent two discrete layers in the aged CC coating.

The impedance responses for as–prepared and aged NCC coating on 2024 aluminium alloy are presented in Figure 11. The frequency dependence of the phase angle presented in Figure 11(b) for as–prepared and aged NCC coating suggests that the CPE may not be applied. As noted by Nguyen et al. [20, 26], the modulus and the ohmic–resistance–corrected phase angle of the as–prepared and aged NCC coating are very similar. The measurement model was fit to the data presented in Figure 11, and the dielectric constant was assumed to be uniform with a value of $\varepsilon = 6.1$, as suggested by Nguyen et al. [26] The resulting resistivity distribution, presented in Figure 12, suggests that the as–prepared and aged NCC coating both showed exponential variation of resistivity. Therefore,
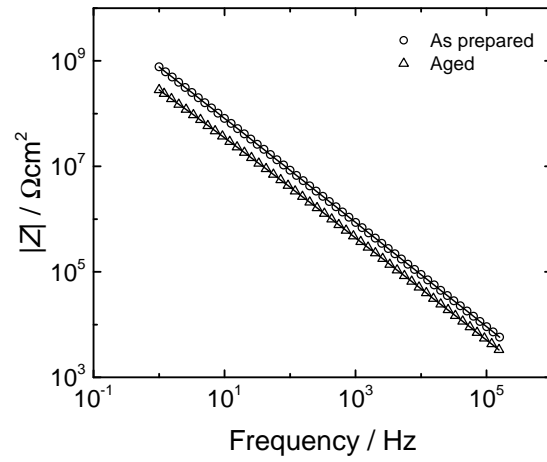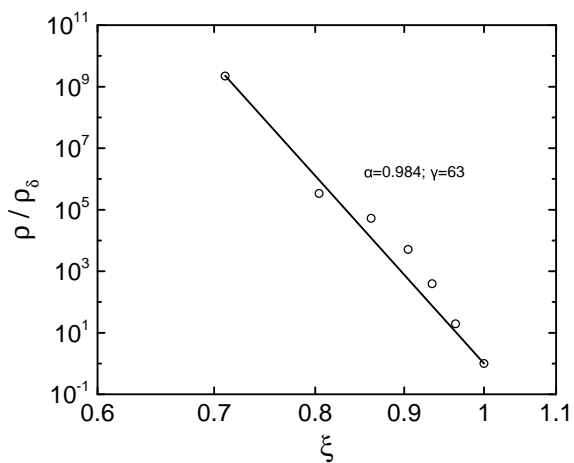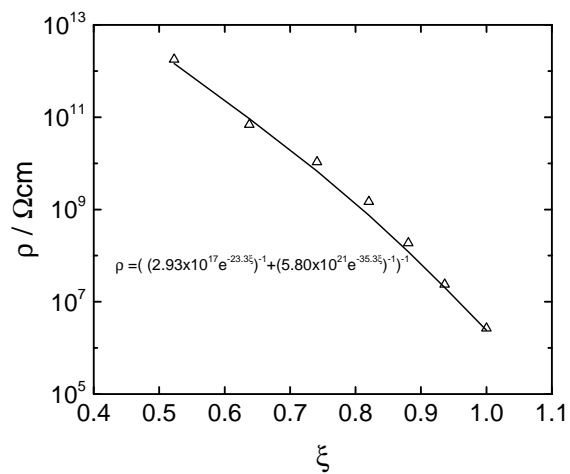
(a)
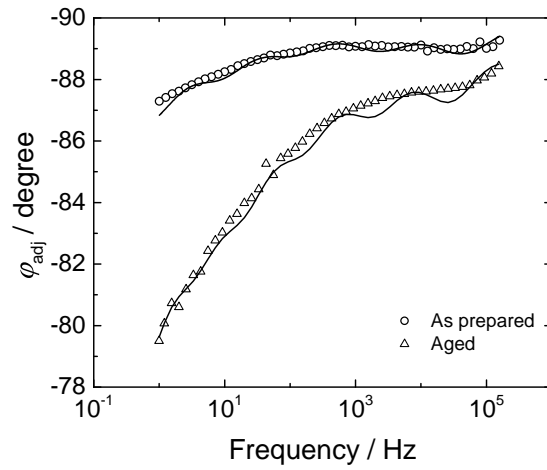
(b)

Figure 9: Measured impedance response for the as–prepared and aged CC coating: a) magnitude of the impedance and b) the ohmic–resistance–corrected phase angle. The line represents the regression of equation (1) to the data.
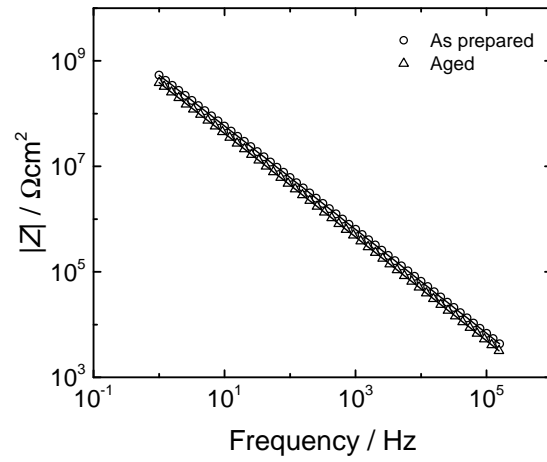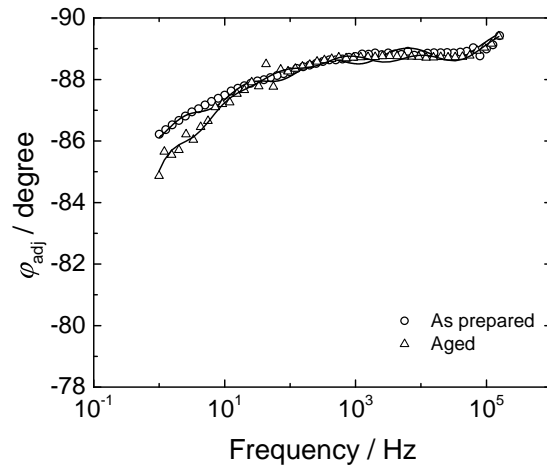
α=0.984; γ=63

(a)

$\rho = (\ (2.93 \times 10^{17} e^{-23.3\xi})^{-1} + (5.80 \times 10^{21} e^{-35.3\xi})^{-1})^{-1}$

(b)

Figure 10: Resistivity as a function of dimensionless position: a) as–prepared in log–log coordinates; and b) aged CC coating in semilog coordinates. The symbols are the discrete resistivity values calculated from equation (6) using the regressed values of τ_i and $\varepsilon = 4.9$.

(a)

(b)

Figure 11: Measured impedance response for the as–prepared and aged NCC coating: a) magnitude of the impedance and b) the ohmic–resistance–corrected phase angle. The line represents the regression of equation (1) to the data.
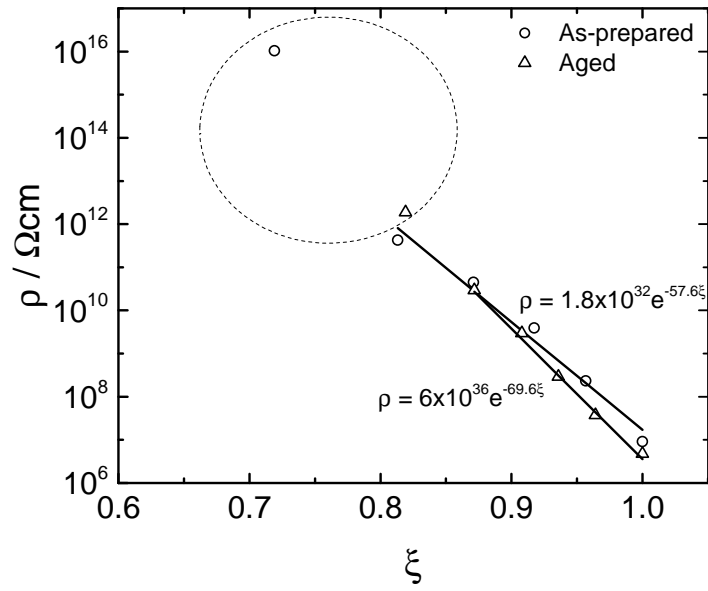
Figure 12: Resistivity as a function of dimensionless position for as prepared and aged NCC coating. The symbols are the discrete resistivity values calculated from equation (6) using the regressed values of τ_i and $\varepsilon = 6.1$. The circled values were not used in the subsequent analysis.

19

Table 4: Results of the measurement model analysis for the experimental data presented in Figures 9 and 11 for CC and NCC coatings, respectively. The value of ρ_0 are larger than expected because the impedance measurements were not performed at frequencies sufficiently low to probe the inner region of the film.

Coating	As–Prepared	Aged
CC	power–law, equation (11)	modified Young, equation (25)
	$\gamma = 63$ $(\alpha = 0.984)$	$\rho_{0,1} = 2.93 \times 10^{17}$ Ωcm; $(\delta/\lambda)_1 = 23.3$
		$\rho_{0,2} = 5.80 \times 10^{21}$ Ωcm; $(\delta/\lambda)_2 = 35.3$
NCC	Young, equation (24)	Young, equation (24)
	$\rho_0 = 1.8 \times 10^{32}$ Ωcm; $(\delta/\lambda) = 57.6$	$\rho_0 = 6 \times 10^{36}$ Ωcm; $(\delta/\lambda) = 69.6$

the Young impedance model applies for the NCC coating. The aging process resulted in a slight decrease in coating resistivity.

The results of the measurement model analysis are presented in Table 4 for the experimental data presented in Figures 9 and 11 for CC and NCC coatings, respectively. In each case, the impedance analysis suggests a variation of resistivity in a region very close to the coating–electrolyte interface. The values of ρ_0 obtained for the aged CC and the as–prepared and aged NCC coatings are larger than expected for a coating. The impedance measurements did not extend to frequencies that were sufficiently low to probe the inner region of the coating.

5. Conclusions

The Voigt measurement model, developed in the 1990s for identification of the error structure of impedance measurements, is shown here to have utility in identifying resistivity distributions that give rise to frequency dispersion. The approach applies for cases where the frequency dispersion may be attributed to a distribution of resistivity through a film on the electrode surface.

The measurement model analysis proposed provides a general explanation for situations in which a distribution of film properties results in frequency dispersion. The method is general and may be used to extract resistivity distribution from impedance data. In the present work, the analysis was validated by application to synthetic data derived from a CPE, a power–law distribution of resistivity, and an exponential distribution corresponding to a Young model. The application to experimental data obtained from coated aluminum demonstrates its utility for interpretation of impedance measurements. The method may be especially useful for analysing experimental results that do not obey one of the mathematically simple $\rho - x$ dependencies previously discussed by Young [2] and Hirschorn et al. [3]

[1] G. J. Brug, A. L. G. van den Eeden, M. Sluyters-Rehbach, J. H. Sluyters, The analysis of electrode impedances complicated by the presence of a constant phase element, Journal of Electroanalytical Chemistry 176 (1984) 275–295.

[2] L. Young, Anodic oxide films 4: The interpretation of impedance measurements on oxide coated electrodes on niobium, Transactions of the Faraday Society 51 (1955) 1250–1260.

[3] B. Hirschorn, M. E. Orazem, B. Tribollet, V. Vivier, I. Frateur, M. Musiani, Constant-phase-element behavior caused by resistivity distributions in films: 1. Theory, Journal of the Electrochemical Society 157 (2010) C452–C457.

[4] L. Young, Anodic Oxide Films, Academic Press, New York, 1961.

[5] C. Bataillon, S. Brunet, Electrochemical impedance spectroscopy on oxide films formed on zircaloy 4 in high temperature water, Electrochimica Acta 39 (1994) 455–465.

[6] M. E. Orazem, B. Tribollet, V. Vivier, S. Marcelin, N. Pébère, A. L. Bunge, E. A. White, D. P. Riemer, I. Frateur, M. Musiani, Dielectric properties of materials showing constant-phase-element (CPE) impedance response, Journal of the Electrochemical Society 160 (2013) C215–C225.

[7] F. Mohammadi, T. Nickchi, M. Attar, A. Alfantazi, EIS study of potentiostatically formed passive film on 304 stainless steel, Electrochimica Acta 56 (2011) 8727–8733.

[8] L. Beaunier, I. Epelboin, J. C. Lestrade, H. Takenouti, Etude electrochimique, et par microscopie electronique à balayage, du fer recouvert de peinture, Surface Technology 4 (1976) 237–254.

[9] F. Mansfeld, Use of electrochemical impedance spectroscopy for the study of corrosion protection by polymer coatings, Journal of Applied Electrochemistry 25 (1995) 187–202.

[10] R. Hirayama, S. Haruyama, Electrochemical impedance for degraded coated steel having pores, Corrosion 47 (1991) 952–958.

[11] V. Upadhyay, U. D. Harkal, D. C. Webster, G. P. Bierwagen, Preliminary investigation of the impact of polymer composition on electrochemical properties of coatings as determined by electrochemical impedance spectroscopy, Journal of Coatings Technology and Research 10 (2013) 865–878.

[12] J. M. Hu, J. Q. Zhang, C. N. Cao, Determination of water uptake and diffusion of Cl^- ion in epoxy primer on aluminum alloys in NaCl solution by electrochemical impedance spectroscopy, Progress in Organic Coatings 46 (2003) 273–279.

[13] T. L. Metroke, J. S. Gandhi, A. Apblett, Corrosion resistance properties of ormosil coatings on 2024-T3 aluminum alloy, Progress in Organic Coatings 50 (2004) 231–246.

[14] J. Kittel, N. Celati, M. Keddam, H. Takenouti, New methods for the study of organic coatings by EIS: New insights into attached and free films, Progress in Organic Coatings 41 (2001) 93–98.

21

[15] J. Kittel, N. Celati, M. Keddam, H. Takenouti, Influence of the coating-substrate interactions on the corrosion protection: Characterisation by impedance spectroscopy of the inner and outer parts of a coating, Progress in Organic Coatings 46 (2003) 135–147.

[16] B. Hinderliter, S. Croll, D. Tallman, Q. Su, G. Bierwagen, Interpretation of EIS data from accelerated exposure of coated metals based on modeling of coating physical properties, Electrochimica Acta 51 (2006) 4505–4515.

[17] S. Amand, M. Musiani, M. E. Orazem, N. Pébère, B. Tribollet, V. Vivier, Constant-phase-element behavior caused by inhomogeneous water uptake in anti-corrosion coatings, Electrochimica Acta 87 (2013) 693–700.

[18] M. Musiani, M. E. Orazem, N. Pébère, B. Tribollet, V. Vivier, Determination of resistivity profiles in anti-corrosion coatings from constant-phase-element parameters, Progress in Organic Coatings 77 (2014) 2076–2083.

[19] V. B. Mišković-Stanković, D. M. Dražić, Z. Kačarević-Popović, The sorption characteristics of epoxy coatings electrodeposited on steel during exposure to different corrosive agents, Corrosion Science 38 (1996) 1513–1523.

[20] A. S. Nguyen, M. Musiani, M. E. Orazem, N. Pébère, B. Tribollet, V. Vivier, Impedance analysis of the distributed resistivity of coatings in dry and wet conditions, Electrochimica Acta 179 (2015) 452–459.

[21] P. Agarwal, M. E. Orazem, L. H. García-Rubio, Measurement models for electrochemical impedance spectroscopy: 1. Demonstration of applicability, Journal of the Electrochemical Society 139 (1992) 1917–1927.

[22] P. Agarwal, O. D. Crisalle, M. E. Orazem, L. H. García-Rubio, Measurement models for electrochemical impedance spectroscopy: 2. Determination of the stochastic contribution to the error structure, Journal of the Electrochemical Society 142 (1995) 4149–4158.

[23] P. Agarwal, M. E. Orazem, L. H. García-Rubio, Measurement models for electrochemical impedance spectroscopy: 3. Evaluation of consistency with the kramers-kronig relations, Journal of the Electrochemical Society 142 (1995) 4159–4168.

[24] F. Dion, A. Lasia, The use of regularization methods in the deconvulation of underlying distributions in electrochemical processes, Journal of Electroanalytical Chemistry 475 (1999) 28–37.

[25] M. E. Orazem, P. K. Shukla, M. A. Membrino, Extension of the measurement model approach for deconvolution of underlying distributions for impedance measurements, Electrochimica Acta 47 (2002) 2027–2034.

[26] A. S. Nguyen, M. Musiani, M. E. Orazem, N. Pèbére, B. Tribollet, V. Vivier, Impedance study of the influence of chromates on the properties of waterborne coatings deposited on 2024 aluminium alloy, Corrosion Science 109 (2016) 174–181.

[27] M. E. Orazem, A systematic approach toward error structure identification for impedance spectroscopy, Journal of Electroanalytical Chemistry 572 (2004) 317–327.

[28] M. Musiani, M. E. Orazem, N. Pébère, B. Tribollet, V. Vivier, Constant-phase-element behavior caused by coupled resistivity and permittivity distributions in films, Journal of the Electrochemical Society 158 (2011) C424–C428.

List of Figures

24

25